Flow (2026), **6** E11
doi:10.1017/flo.2026.10048

FLOW CAMBRIDGE UNIVERSITY PRESS

RESEARCH ARTICLE

Control of stationary cross-flow instabilities using periodic arrays of spanwise-invariant roughness strips

Giulia Zoppini, Marios Kotsonis and Theodoros Michelis

Faculty of Aerospace Engineering, Delft University of Technology, Delft 2629 HS, The Netherlands
Corresponding author: Theodoros Michelis; Email: t.michelis@tudelft.nl

Received: 15 October 2025; **Revised:** 5 February 2026; **Accepted:** 18 March 2026

Keywords: crossflow instability; laminar to turbulent transition

Abstract

This study examines the control capabilities of an array of spanwise-invariant roughness strips applied on a swept-wing boundary layer (BL) dominated by a cross-flow instability (CFI) that is forced by periodically spaced discrete roughness elements to a monochromatic wavelength. Several configurations of strip arrays are investigated, varying their height, width and chordwise periodicity. Infrared thermography is employed to track the impact on the BL transition location. Optimal configurations are identified, extending laminar flow by up to 10 % of the wing chord. Additionally, BL forced by patches of randomised surface roughness are considered, better representing realistic wing surfaces. In this scenario, the application of strip arrays with optimal geometry extends the laminar portion of the BL by almost 10 % chord and beyond when combined with a discrete roughness element array. Time-averaged particle image velocimetry (PIV) velocity fields are acquired to monitor the CFI amplitude for the various configurations. The BL spectral content in the spanwise direction is used to characterise the chordwise behaviour of individual disturbance modes, whose amplitude is found to be reduced by up to 17 % for the optimal strip configuration.

Impact statement

This study demonstrates that spanwise-invariant periodic roughness configurations can effectively delay boundary-layer transition in swept-wing flows dominated by cross-flow instability (CFI). By systematically varying roughness geometry – height, width and chordwise spacing – optimal configurations are identified that extend laminar flow by up to 10 % of the aerofoil chord. Under both idealised and realistic surface conditions with randomised roughness, infrared thermography and velocity-field measurements reveal suppressed CFI amplitudes and altered spanwise spectral content. The results show up to a 17 % reduction in chordwise growth of instability modes. Combining roughness strip arrays with discrete roughness elements (DREs) further enhances control, demonstrating scalability to practical aerodynamic conditions. These findings establish a foundation for passive flow-control strategies that delay transition, offering a robust and low-cost path to improved aerodynamic efficiency in real-flight applications.

1. Introduction

On a swept wing subject to favourable pressure gradient, laminar to turbulent transition is governed by cross-flow instabilities (CFIs) which, in low free-stream turbulence environments, manifest as stationary,

co-rotating vortices, closely aligned with the free-stream direction (Bippes 1999; Saric *et al*. 2003; Serpieri & Kotsonis 2016). The onset and evolution of stationary CFIs are highly sensitive to surface roughness (Müeller & Bippes 1989; Deyhle & Bippes 1996; Radeztsky *et al*. 1999; Saric *et al*. 2003). To induce a monochromatic CFI mode, artificial forcing with a periodic array of discrete roughness elements (DREs) parallel to the leading edge has often been employed (Radeztsky *et al*. 1999; Saric *et al*. 2003; Serpieri & Kotsonis 2016). At the same time, Saric *et al*. (1998) demonstrated that sub-critical forcing (using a DRE array whose wavelength is shorter than the critical CFI wavelength, λ_{crit}) can inhibit the growth of the most unstable modes and delay laminar-to-turbulent transition.

Previous studies have demonstrated that control methods built on wave superposition principles can successfully control boundary layers for which transition is dominated either by Tollmien–Schlichting (TS) waves (e.g. Milling 1981; Tol *et al*. 2019*b*) or by CFI (e.g. Wassermann & Kloker 2000; Zoppini *et al*. 2022*a*). In both cases, during the initial exponential growth phase, modes develop independently from each other (i.e. free from non-linear interactions (Bippes 1999; Saric *et al*. 2003; Schlichting & Gersten 2017; Schubauer & Skramstad 1947)). Therefore, artificially introduced monochromatic disturbances with optimal amplitude and phase shift can be employed without causing significant mode coupling, effectively damping instability growth. In two-dimensional (2-D) scenarios, this has led to the development of adaptive control systems capable of damping TS waves at various locations (Baumann *et al*. 2000; Ladd 1990; Sturzebecher & Nitsche 2003; Tol *et al*. 2019*a*). In contrast, in three-dimensional (3-D) scenarios, upstream flow deformation (UFD) techniques are implemented in combination with classical BL suction to optimise the location, arrangement and strength of multiple suction orifices, inhibiting primary CFI growth and delaying secondary instabilities (Friederich & Kloker 2012; Messing & Kloker 2010).

Recent investigations have explored the use of passive surface-embedded resonators for controlling TS waves relying either on the excitation of elastic waves within the sub-surface (e.g. Barnes *et al*. 2021; Hussein *et al*. 2015; Park *et al*. 2022; Michelis *et al*. 2023*b*) or the acoustic response of Helmholtz resonators (Michelis *et al*. 2023*a*). The frequency dispersion of the aforementioned resonators can be tailored accordingly such that the interface interferes constructively or destructively with the TS waves, leading to the formation of pass bands or stop bands respectively. While the TS attenuation achieved is modest, the localised scattering effect (Dong & Wu 2016; Xu *et al*. 2016) suggests that a properly tuned series of such devices could significantly enhance overall control capabilities over the surface.

Drawing inspiration from the above, to attenuate the development of CFI in a 3-D boundary layer, a passive laminar flow control technique based on the application of a streamwise series of DRE arrays with optimal amplitude and phase arrangement has been investigated by Zoppini *et al*. (2022*a*). These surface roughness modifications introduce velocity disturbance systems that destructively interfere with the developing CFI through a wave superposition process, significantly reducing its amplitude and delaying BL transition. However, the potential of the proposed cancellation technique is limited by its strong sensitivity to external disturbances, particularly in scenarios with enhanced distributed surface roughness. This behaviour is mostly attributed to the lack of control on the phase shift between pre-existing CFI and the introduced velocity disturbances, resulting in the persistence of residual small-wavelength CFI modes in the boundary layer. In a similar vein, Ivanov *et al*. (2018) reported that oblique surface non-uniformities on a swept wing can either amplify or attenuate the growth of cross-flow vortices, depending on their orientation relative to the leading edge. Specifically, stabilisation occurs when the non-uniformities are aligned parallel to the leading edge. Furthermore, a direct correlation was observed between the number of non-uniformities and the magnitude of the stabilising or destabilising effect, with stronger effects arising as their number increases.

Despite these advancements, to the authors' best knowledge, other than the aforementioned works, no attempts have been made to stabilise stationary CFI using arrays of periodic units in 3-D BL scenarios, specifically focussing on possible scattering behaviour. This study aims to fill this gap by experimentally investigating the interaction between stationary CFI on a swept wing BL and a spanwise-invariant roughness strip array (SA). Various design parameters are explored to optimise the roughness geometry, with a primary focus on the effect of the array periodicity on BL development. The effectiveness

https://doi.org/10.1017/flo.2026.10048 Published online by Cambridge University Press

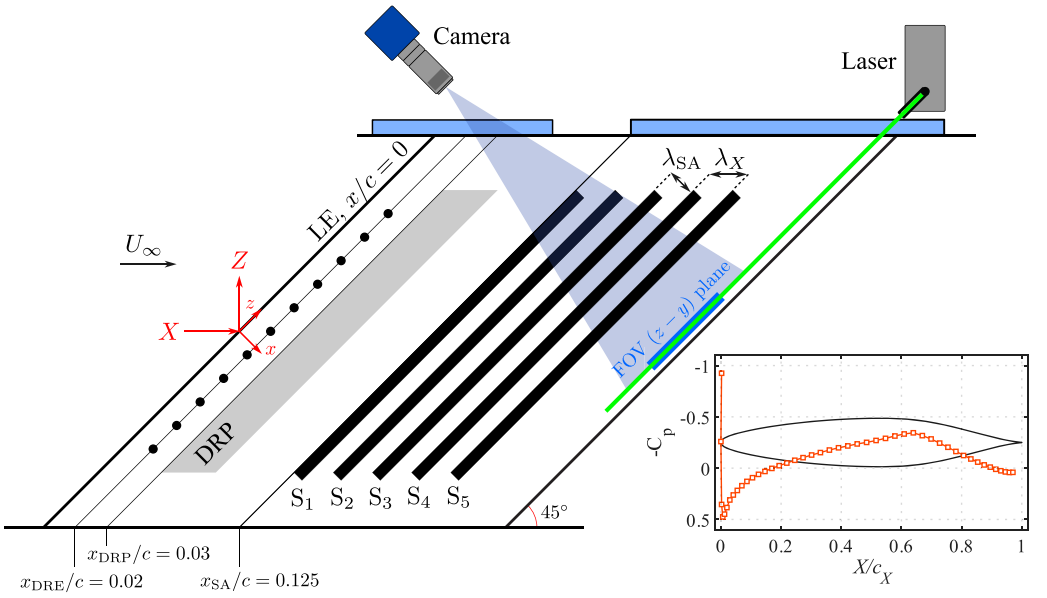

Figure 1. *Schematic of the experimental set-up (not to scale) with the various roughness configurations; strip array (SA) and distributed roughness patch (DRP). The right panel depicts the aerofoil shape along X (to scale) and the corresponding pressure coefficient at the experiment conditions.*

of the SA is evaluated in both a boundary layer forced by a reference DRE array as well as in the presence of randomised distributed roughness (Kendall 1981; Suryanarayanan *et al*. 2020; Zoppini *et al*. 2022*a*). The former results in the development of monochromatic CFI with periodicity corresponding to the DRE forcing wavelength, spanning from sub-critical ($\lambda < \lambda_{crit}$), critical ($\lambda = \lambda_{crit}$) to super-critical ($\lambda > \lambda_{crit}$). Conversely, the latter induces more realistic conditions, reflecting a rougher wing surface finish, and leads to a BL with broader spectral content, including the simultaneous development of various CFI modes.

2. Methodology

2.1. Wind tunnel and wing model

The presented work is carried out in the low speed Low Turbulence Tunnel (LTT) of TU Delft ($T_u/U_\infty \simeq 0.025$ %, in the range 25–60 ms^{-1}, bandpassed between 2 Hz and 5000 Hz, Serpieri 2018), on a constant-chord ($c_X = 1.27\mathrm{m}$, along X) swept (45°) wing model (M3J, Serpieri & Kotsonis 2015; Serpieri 2018) with smooth surface ($R_q = 0.2\,\mu\mathrm{m}$). The model is designed to ensure that stationary CFI dominates the BL evolution and transition, providing a favourable pressure gradient up to 65 % chord. Measurements are performed on the pressure side of the wing model at angle of attack $\alpha = -3.4°$ and Reynolds number $\mathrm{Re}_{c_x} = 2.17 \times 10^6$ ($U_\infty = 25.6\ \mathrm{ms}^{-1}$). An overview of the experimental set-up is shown in Figure 1. Two different coordinate systems are used throughout this work: the first is integral to the wind tunnel floor, with spatial components X, Y, Z and velocity components U, V, W, and is employed for the analysis of the acquired infrared images; the second is a wall-attached, curvilinear, coordinate system, integral to the swept wing, with the z-axis aligned to the leading edge, while the x-axis and y-axis are parallel and normal to the local surface tangent, respectively. Corresponding body-fitted velocity components u, v, w are extracted from particle image velocimetry (PIV) measurements. At this angle of attack, spanwise pressure gradient uniformity was found to be excellent (Serpieri & Kotsonis 2015); hence, no wall liners were necessary to treat the wind tunnel walls (see e.g. Deyhle & Bippes 1996).

https://doi.org/10.1017/flo.2026.10048 Published online by Cambridge University Press

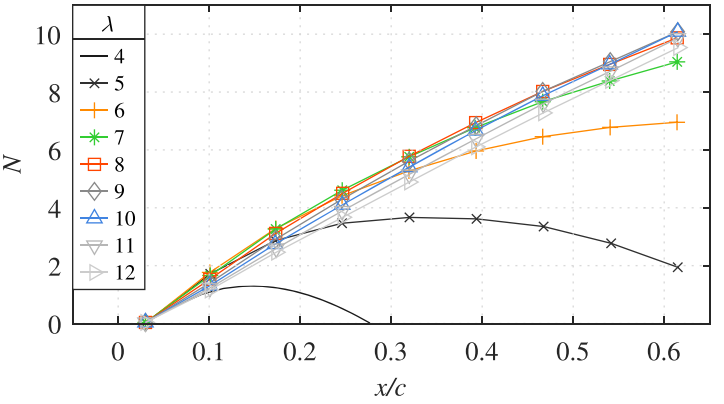

Figure 2. *Linear stability analysis amplification factor (N) of the unforced BL for a set of stationary modes with λ ranging from 4 mm to 12 mm.*

2.2. Surface roughness features

2.2.1. Discrete roughness element (DRE) arrays

At the aforementioned experimental conditions, linear stability theory predictions based on in-house solutions of the Orr–Sommerfeld equation (Mack 1984) and previous work from the authors (Serpieri & Kotsonis 2015) confirm that the critical modes lie in the range of 8–10 mm for a smooth wing without surface modifications. Discrete roughness element (DRE) arrays are applied at $x_{\mathrm{DRE}}/c = 0.02$ to ensure the development of a monochromatic CFI mode (e.g. Radeztsky *et al*. 1999; Saric *et al*. 2003). A critical DRE array with element inter-spacing of $\lambda_f = \lambda_1 = 8\,\mathrm{mm}$ provides the reference baseflow BL for the majority of the presented cases, ensuring that the CFI attains measurable amplitude downstream of $x/c = 0.1$. Nevertheless, based on linear stability analysis (Figure 2), the SA is anticipated to also interact with cross-flow instabilities of wavelengths other than the forced critical one. To confirm if this is the case, sub-critical ($\lambda_f = 6\,\mathrm{mm}$), near-critical ($\lambda_f = 7\,\mathrm{mm}$) and super-critical ($\lambda_f = 10\,\mathrm{mm}$) baseflow configurations are also considered.

All DRE arrays (see Table 1 for properties) are manufactured in-house and geometrically characterised as described by Zoppini (2023), by knife cutting a PVC foil with nominal height of $k = 70\,\mu\mathrm{m}$. Each DRE is designed to feature a cylindrical shape with diameter $d = 2\,\mathrm{mm}$. To ensure no major shape and height variations occur due to the manufacturing process, a statistical characterisation of their geometric properties is performed. Sub-samples of the arrays are scanned with a scanCONTROL 30xx profilometer, operating with a semiconductor laser with a 405 nm wavelength and $1.5\,\mu\mathrm{m}$ reference resolution. The data acquisition and processing is described by Zoppini *et al*. (2022*b*), resulting in an effective element height of $k = 0.0843 \pm 0.0003\,\mathrm{mm}$ and diameter $d = 2.03 \pm 0.0013\,\mathrm{mm}$ for the current application (Figure 3).

2.2.2. Distributed surface roughness patches (DRPs)

Typically, the surface finishing of commercial air vehicles results in a distributed surface roughness with an average height of $\simeq 11\,\mu\mathrm{m}$ (Boeing 2013). Therefore, to mimic background surface roughness, distributed roughness patches (fine silicon carbide) are applied on the wing, resulting in a random distribution of local roughness peaks, as characterised by Zoppini *et al*. (2022*a*). The resulting DRP average height is $k_{\mathrm{DRP}} \simeq 0.010 \pm 0.001\,\mathrm{mm}$, with local peak heights reaching a maximum value of approximately 0.04 mm (Figure 4a). The DRP amplitude distribution is characterised by a broadband spanwise spatial content in the range of $0{-}2\lambda_1$ (Figure 4b). Hence, it is expected that the DRP will excite a set of CFI modes with various spanwise wavelengths within the same range, resulting in a BL containing simultaneously developing small wavelength CFI (Saric *et al*. 2011; Zoppini *et al*. 2022*a*). Throughout

https://doi.org/10.1017/flo.2026.10048 Published online by Cambridge University Press

Table 1. *Nominal geometric parameters of the DRE arrays and DRP and the respective transition location*

Name	k/mm	d/mm	λ_f/mm	λ_X/mm	λ/λ_1	λ_X/λ_1	x/c	k/δ^*	Re_k	$x_{\mathrm{TR,b}}/c$
A6	0.07	2	6	6.9	0.75	1.15	0.02	0.125	7	0.56
A7	0.07	2	7	8.0	0.87	1.15	0.02	0.125	7	0.47
A8	0.07	2	8	9.2	1	1.15	0.02	0.125	7	0.35
A10	0.07	2	10	11.5	1.25	1.15	0.02	0.125	7	0.36
DRP	0.01	–	0–16	–	0–2	–	0.03	0.017	0.2	0.37

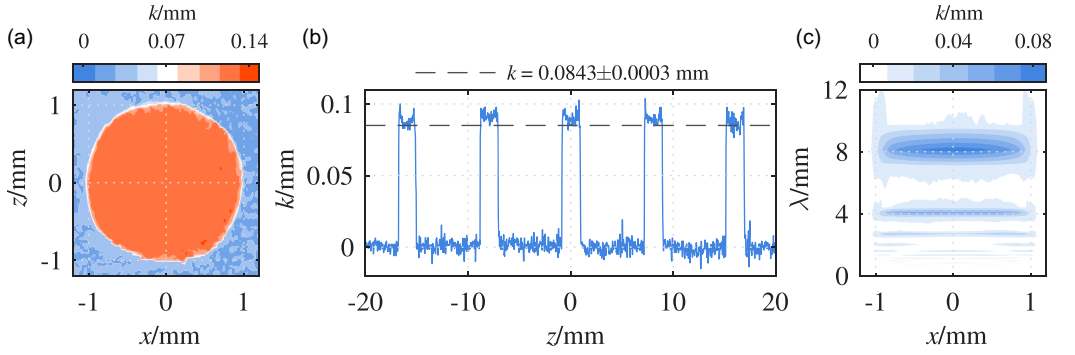

Figure 3. *Statistical characterisation of a DRE array: (a) height map of a representative DRE element; (b) slice of the height map along the centreline of the DRE array; (c) spatial spectrum of the DRE array.*

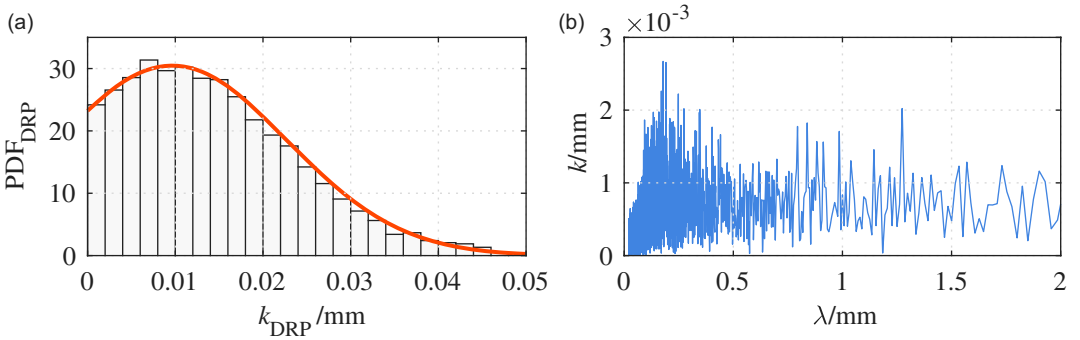

Figure 4. *Statistical characterisation of a sample DRP: (a) typical histogram of a DRP heightmap showcasing the distribution of roughness height; (b) a representative wavelength spectrum of the DRP.*

this work, the cases combining elevated background roughness and other roughness manipulations (i.e. DRP and SA or DRP, DRE and SA) feature the same DRP located at $x_{\mathrm{DRP}}/c = 0.03$ (see Figure 1).

2.2.3. Spanwise-invariant roughness Strip Arrays (SAs)

Spanwise-uniform roughness strip arrays (SAs) are designed to attenuate the CFI developing in the reference BL. Unlike traditional 2-D BL control methods, this approach targets stationary, wave-like CFI patterns along the chord-wise (streamwise) direction, matching the instability's spatial periodicity. This is reminiscent of the work by Justiniano *et al*. (2024) and Suryanarayanan *et al*. (2020) on distributed roughness shielding in unswept flows dominated by streaky structures. The SA, therefore, operates parallel to the instability propagation direction, contrasting with transverse (wall-normal) approaches for Tollmien–Schlichting wave attenuation (Hussein *et al*. 2015; Michelis *et al*. 2023*a*).

https://doi.org/10.1017/flo.2026.10048 Published online by Cambridge University Press

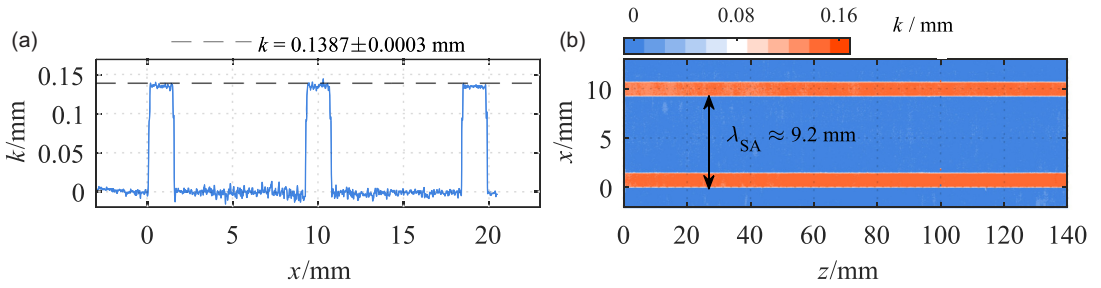

Figure 5. *Characterisation of the roughness strip array: (a) representative slice of strip height; (b) height map of two representative strips.*

Several considerations are factored in the SA design. For representative measurements, they must be applied in the region of the BL where CFIs are already exponentially amplified, yet not saturated, as to avoid the insurgence of secondary instabilities and laminar breakdown. Based on previous investigations (Zoppini *et al*. 2022*a*), for the present set-up, the chord location combining these two requirements is $x/c = 0.125$. For similarity with the employed DRE arrays, the individual strips are designed such that they are parallel to the leading edge, with predefined nominal height and width of $k_{SA} = 0.07\,\mathrm{mm}$ and $w_{SA} = 2\,\mathrm{mm}$, respectively. The SA location (i.e. x_{SA}/c) is defined as the location of the first strip on the wing (set to $x/c = 0.125$), while the number of strip units in each SA (N_{SA}) is applied with set streamwise periodicity. This characteristic wavelength is set to match the streamwise wavelength of the dominant CFI (λ_X), which is determined during preliminary IR investigation of the DRE-forced BL to be $9.2\,\mathrm{mm}$ at $x/c = 0.125$.

SAs are manufactured in-house by knife cutting PVC foils of nominal height between 0.07 mm and 0.17 mm. The procedure is analogous to the DRE cutting, with each SA being produced as a single piece to be pasted on the wing. A reference sample is laser-scanned to assess the effective geometry, of nominal values for height, width and periodicity of $k_{SA} = 0.14\,\mathrm{mm}$, $w_{SA} = 2\,\mathrm{mm}$ and $\lambda_{SA} = 9.2\,\mathrm{mm}$, respectively (Figure 5).

2.3. Measurement techniques

2.3.1. Infrared thermography

Infrared (IR) thermography employs radiometric sensors located outside of the wind tunnel test section, allowing non-intrusive imaging of the wing surface temperature. Based on the Reynolds' analogy (Reynolds, 1883), higher temperature regions in the IR image are associated with laminar flow, while lower temperature regions correspond to turbulent flow (Bippes 1999; Dagenhart & Saric 1999; Serpieri 2018). Therefore, an IR image offers a global overview of the flow field, and provides the location and topology of the BL laminar-to-turbulent transition.

In the current investigation, an Optris PI640 IR camera images the wing pressure side at the chosen flow conditions (i.e. $\mathrm{Re}_c = 2.17 \times 10^6$ and $\alpha = -3.4°$) for the various roughness configurations considered. The acquired domain is centred at the wing midspan and imaging with spatial resolution of $\simeq 1.7\,\mathrm{mm\,px^{-1}}$. Given the stationary nature of the investigated flow features, for each configuration, 80 images are acquired at a frequency of 4 Hz and are averaged to reduce the image-to-noise ratio. The thermal contrast between laminar and turbulent flow regions is enhanced by external surface heating provided by IR-optimised halogen lamps (3×400 W and 2×500 W). The model temperature increase occurring throughout the measurement is within 4 % of the measured flow temperature (in K); hence, any effect the BL transition location is negligible, as also observed in previous experimental investigations (Lemarechal *et al*. 2019). The averaged IR images (Figure 6) are geometrically mapped to the

https://doi.org/10.1017/flo.2026.10048 Published online by Cambridge University Press

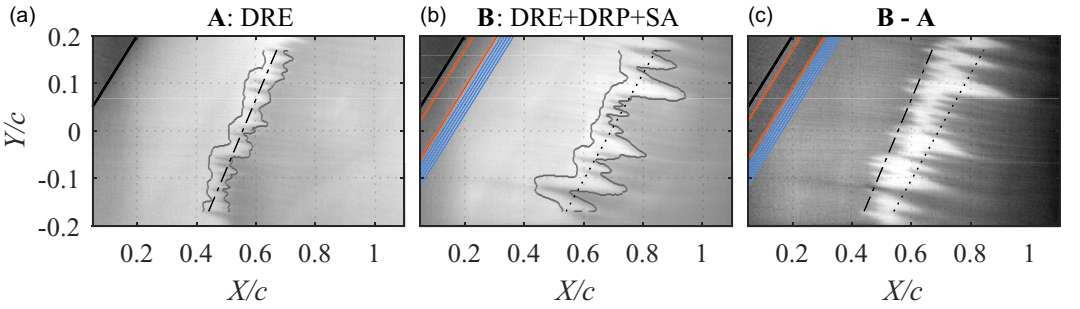

Figure 6. *Exemplary infrared images for: (a) DRE forced BL; (b) DRE/DRP/SA forced BL; (c) differential result, the bright area exhibiting the extent of transition delay. Aerofoil leading edge (——); extent of DRP (——); SA units (——); transition region identified with Gabor filtering (——); linear fit of transition region (- · - · -, ·····) that defines x_{TR} along the span.*

tunnel-attached reference system, X, Y, Z, and are post-processed through an in-house developed routine that locally identifies the absolute transition location (x_{TR}) on the surface of the wing by means of Gabor filtering (Gabor 1946; Michelis *et al*. 2024).

2.3.2. Planar particle image velocimetry (PIV) and vector field processing

Particle image velocimetry (PIV) is used to locally quantify the BL flow characteristics and its chordwise development under different forcing configurations along the $z-y$ plane (i.e. spanwise wall-normal) at a fixed chord location, $x/c = 0.25$ (Figure 1). The z and y coordinates are normalised by $\lambda_1 = 8\,\mathrm{mm}$ and the experimentally determined displacement thickness on the $z-y$ plane at $x/c = 0.3$ ($\delta^*_w = 0.72\,\mathrm{mm}$), respectively. Illumination is provided by a Quantel Evergreen Nd:YAG dual cavity laser (200 mJ per pulse at $\lambda = 532\,\mathrm{nm}$). A set of optics is used to transform the beam to a sheet of approximately 1 mm thickness. Imaging is performed with a LaVision Imager camera (sCMOS, 2560×2160 pixels, 16-bit, $6.5\,\mu\mathrm{m}$ pixel pitch) equipped with a 200 mm objective ($f_{\#} = 8$) and a 2× tele-converter to attain the field of view (35 mm × 10 mm). Seeding is obtained by dispersing $0.5\,\mu\mathrm{m}$ droplets of water–glycol mixture through a SAFEX fog generator. Each image pair ($\Delta t = 15\,\mu\mathrm{s}$) is processed in LaVision Davis 10, employing a 2-frame particle tracking (PTV) algorithm to identify particle trajectories, which are then spatially binned ($6 \times 6\,\mathrm{px}^2$) and converted to a 500×140 Cartesian grid with a vector pitch of $80\,\mu\mathrm{m}$.

Time-averaged spanwise and wall-normal velocity fields ($\overline{w}, \overline{v}$) are further processed to extract the main flow features. The spanwise-average of $\overline{w}$ is used to define the baseline mean BL velocity profile $\overline{w}_{\mathrm{b}}$ at $x/c = 0.30$. This provides an estimate of the free-stream spanwise velocity, W_∞, indicating that the employed optical set-up and processing resolve the BL up to $\overline{w} = 1.4\,\%W_\infty$, with local uncertainty of 0.6 % within the BL and 0.04 % in the free stream. The $\overline{v}$ component is resolved up to $\overline{v} = 1.4\,\%V_\infty$, with local uncertainty of 4 % within the BL and 0.04 % in the free stream. By subtracting the $\overline{w}_{\mathrm{b}}$ profile from $\overline{w}$, the disturbance velocity field, $\overline{w}_{\mathrm{d}}$, is obtained. The standard deviation of $\overline{w}$ along the spanwise direction can, instead, provide an estimation of the disturbance profile along the y direction, $\langle \overline{w} \rangle_z$ (see e.g. Hunt & Saric 2011; Reibert *et al*. 1996; Tempelmann *et al*. 2012).

Spatial fast Fourier transform (FFT) analysis is performed to infer the spectral organisation of the flow field: at each y coordinate, the spanwise $\overline{w}_{\mathrm{d}}$ signal is transformed to the spatial frequency domain, providing information on the modal composition of the developing BL and on the evolution of the individual Fourier modes. Such FFT analysis also provides fundamental information regarding the phase of the individual modes, which is fundamental to establish the SA effect on the flow field. Moreover, the local CFI amplitude (A_{int}) is estimated following the integral amplitude definition (Downs & White 2013). More specifically, the disturbance profiles $\langle \overline{w} \rangle_z$ or the FFT shape functions corresponding to a single

https://doi.org/10.1017/flo.2026.10048 Published online by Cambridge University Press

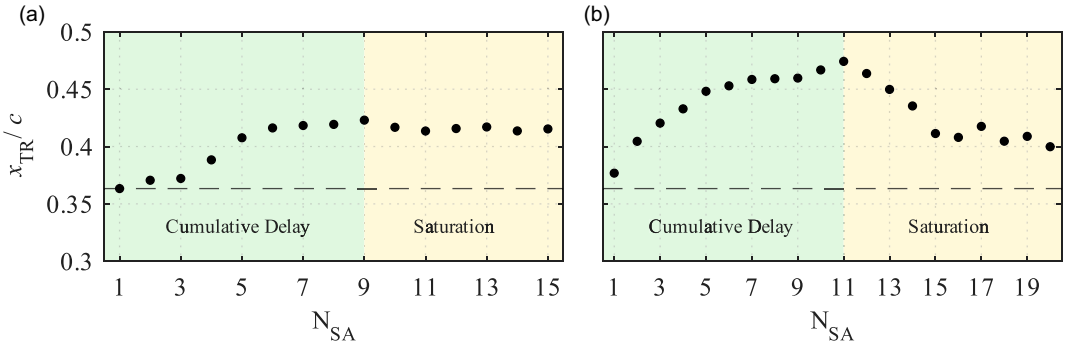

Figure 7. *Variation of x_{TR}/c as a function of SA unit number, extracted from infrared (IR) images compared with the baseline configuration (- - -): (a) $k_{SA} = 0.07$ mm; (b) $k_{SA} = 0.14$ mm.*

mode are integrated along y up to the experimentally determined (PIV) boundary layer edge on the $z-y$ plane ($y = \delta_{99}$), to quantify the CFI chord-wise evolution.

3. Identification of suitable SA geometric parameters

Variations of the preliminary defined reference SA geometry (i.e. DRE forcing and SA, see § 2.2.3) are considered in an exploratory parametric study performed to assess their effect on the flow development. The flow parameters of interest are the number of units, N_{SA}, as well as unit amplitude (i.e. height), k_{SA}, position with respect to chord location, x_{SA}/c, and width, w_{SA}.

The influence of number of strips, N_{SA}, is investigated considering 15 individual strips with reference geometrical features (i.e. $k_{SA} = 0.07$ mm, $\lambda_x/\lambda_1 = 1.15$, $x_{SA}/c = 0.25$, and $w_{SA} = 2$ mm). Individual units are incrementally added, estimating the BL transition location following the addition of each element. Figure 7a illustrates that maximum transition delay is achieved for $N_{SA} = 6$, while $N_{SA} = 5$ suffices to exhibit notable transition delay authority. Further addition of units yields limited effects on the BL transition location, suggesting the onset of a saturation effect.

Similar behaviour is observed when doubling the SA amplitude and increasing the number of units ($k_{SA} = 0.14$ mm, $N_{SA} = 20$), as can be seen in Figure 7b. With these taller elements, cumulative transition delay is achieved up to $N_{SA} = 11$, possibly due to a more favourable relationship between BL thickness and k_{SA} at downstream chord locations. Nevertheless, significant control capability is evident even when $N_{SA} = 5$, while $N_{SA} \geq 11$ results in a reduction to the achieved transition delay before reaching saturation. This behaviour is indicative of the presence of competing flow mechanisms governing the interaction between the BL and the SA, the identification of which is the subject of ongoing investigations.

The influence of the parameters of SA amplitude (k_{SA}), chord location (x_{SA}/c) and width (w_{SA}) on the transition location is shown in Figure 8. As seen in Figure 8a, all forcing amplitude cases exhibit significant transition delay. Notably, an SA with elements of amplitude $k_{SA} = 0.14$ mm achieves laminar flow extension by nearly 10 % of the chord length. In turn, variation of the streamwise location of the first SA unit (x_{SA}/c) is examined for an SA height of $k_{SA} = 0.07$ mm to avoid the possibility of inducing flow tripping at upstream chord locations. The resulting transition locations are illustrated in Figure 8*b* and indicate that the reference chord-wise location, $x_{SA}/c = 0.125$, appears optimal, while both upstream and downstream shifts of the control configuration are detrimental to the control authority. Finally, as seen in Figure 8c, variation of each unit's width indicates that $w_{SA} = 2$ mm (comparable to the diameter of the DRE elements) provides the most significant transition delay.

For a roughness configuration composed of critical DREs and SAs, the maximum transition delay is obtained at $k_{SA} = 0.14$ mm. This value is therefore adopted as the baseline SA geometry for a

https://doi.org/10.1017/flo.2026.10048 Published online by Cambridge University Press

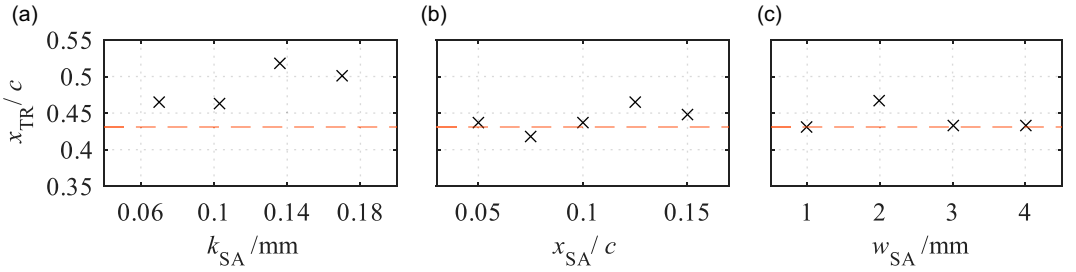

Figure 8. *Transition location, x_{TR}, extracted from IR images for the combination of the baseline configuration (A8, - - -) with a control configuration comprising an SA with 5 units of varying: (a) amplitude; (b) chord location of the first unit; and (c) width.*

width of $w_{SA} = 2\,\mathrm{mm}$. Moreover, given that numerous forcing and control configurations are examined, it is advantageous to use a limited number of units to facilitate both application and removal. Consequently, SAs consisting of five units ($N_{SA} = 5$) are employed; the array starting at $x_{SA}/c = 0.125$. These geometrical characteristics are retained throughout the remainder of this study. Note that preliminary investigations at a range of Reynolds numbers (1.8×10^6–2.6×10^6) led to the same conclusions, with the difference that the the strip array wavelength was scaled to the respective critical wavelength. Consequently, this report focusses on a single Reynolds number (2.17×10^6).

4. Influence of SA periodicity under different roughness configurations

As mentioned earlier, due to the highly polished surface of the M3J wing and low free-stream turbulence intensity of the LTT facility, BL-forcing via DRE or DRP configurations is necessary for achieving laminar–turbulent transition upstream of the wing's pressure minimum. Independent of forcing configuration, the measured IR field as well as the PIV flowfields confirm that transition is dominated by growth and breakdown of stationary CFI. The results presented in this section cover a wide variety of forcing and control configurations; therefore, it is worth clarifying that within this work, a forcing configuration is composed by a single DRE array or DRP, and provides the baseline BL flow and transition location ($x_{TR,b}$). The control configuration is obtained by adding an SA with specific λ_{SA}, resulting in the controlled transition location (x_{TR}). The transition front location and its modifications are discussed in a differential framework: namely, for each control case, $\Delta x_{TR}/c$ is computed as $(x_{TR} - x_{TR,b})/c$. This framework is necessary because, given the extent of the parameter space, the DREs had to be replaced multiple times, requiring back-and-forth changes between DRE wavelengths. As a result, due to the proximity of the DREs to the leading edge, the exact positions of $x_{TR,b}$ for a given DRE wavelength was not identical across all cases, but varied within $0.1c$. The average values are summarised in Table 1.

4.1. DRE-forced boundary layer

All SA configurations applied in a DRE-forced BL result in a significant delay of the transition location, as seen in Figure 9. When applied in a sub-critically forced BL (A6), SAs of any of the considered λ_{SA} are capable of delaying transition up to $x/c \simeq 0.65$, where the aerofoil pressure coefficient reaches its peak value (Serpieri 2018). Due to the pressure gradient becoming adverse at this location, the BL transition in these cases cannot be attested to CFI breakdown, rather it is driven by laminar separation. Furthermore, for the considered Re_c, the forced sub-critical CFI mode (i.e. 6 mm) stabilises downstream of $x/c \simeq 0.35$ (see Figure 2); therefore, damping this sub-critical CFI mode for a long enough portion of the wing chord is sufficient to prevent its growth to saturation and breakdown levels. At the same time, the forcing and initial growth of the sub-critical CFI mode inhibits the onset and development of critical modes (Saric *et al*. 1998; Wassermann & Kloker 2002).

https://doi.org/10.1017/flo.2026.10048 Published online by Cambridge University Press

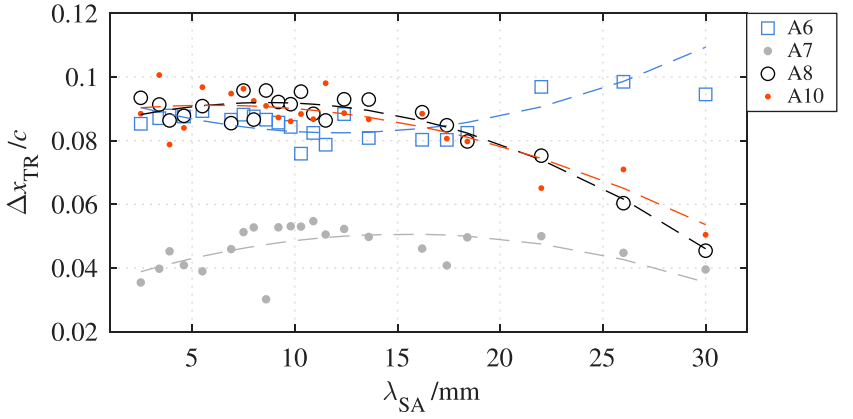

Figure 9. *$\Delta x_{\mathrm{TR}}/c$ extracted from IR images for the combination of a baseline forcing configuration (A6, A7, A8 or A10) and a control configuration featuring SAs of various periodicities, λ_{SA}. Dashed lines correspond to a second-order polynomial fit.*

Furthermore, Figure 9 shows that BLs forced by near-critical (A7), critical (A8) and super-critical (A10) DRE arrays are more sensitive to the SA periodicity, λ_{SA}, yet not all are as effective. More specifically, for near-critical forcing, overall reduced transition delay with respect to the sub-critical baseflow BL is observed, while for the critical and super-critical cases, the laminar flow region is extended by almost 10 % chord for an SA of optimal periodicity. All three forcing cases are more sensitive to the range of SA periodicity between 8 mm and 11.5 mm, comparing well to the range of streamwise wavelengths of the forced (and dominant) CFI modes ($\lambda_x = 8.0\,\mathrm{mm}$, 9.2 mm and 11.5 mm, respectively).

Although it does not fully describe the transitional behaviour, a simple least-squares quadratic fit adequately captures the main variations of $\Delta x_{\mathrm{TR}}/c$ induced by changes in λ_{SA} (see Figure 9). From this fit, the periodicity of the maximum transition delay for each forcing configuration can be estimated by locating the apex of the curve. The resulting values of λ_{SA} are 12.2, 14.5, 8.5 and 8.3 for A6, A7, A8, and A10, respectively.

4.2. DRP-forced and DRE/DRP-forced boundary layer

Considering the evident control capabilities demonstrated by SA arrays applied in DRE-forced BLs, their effectiveness is also investigated for BLs with increased background roughness. As mentioned earlier in this report, to enhance the roughness of the model surface, a distributed roughness patch (DRP) is applied at $x_{\mathrm{DRP}}/c = 0.03$ to force the simultaneous development of multiple stationary CFI modes, resembling more realistic conditions. DRP forcing alone (without DREs) results in BL transition at $x/c \simeq 0.4$, while the transition location change obtained by adding SAs of various wavelengths is shown in Figure 10.

Owing to the loss of monochromatic periodicity in the BL, the $\Delta x_{\mathrm{TR}}/c$ achieved by the DRP and SA combination is more widespread than the respective observations in the previously discussed DRE-forced BL cases. Nonetheless, also in the presence of the DRP, a quadratic fit captures the overall behaviour of the controlled cases, with an apex at $\lambda_{\mathrm{SA}} = 15.3$. Yet, it is observed that for SAs with periodicity in the vicinity of 8 mm, transition delay is more effective, as wavelengths developing in the DRP case are expected to be at a wavelength range comparable to the critical one.

Building on this, the performance of critical-periodicity SAs in configurations combining simultaneous forcing with DRE arrays and DRP is also investigated. In these set-ups, the DRE array is placed upstream of the DRP at $x/c = 0.02$ to impose a monochromatic CFI mode in the leading-edge region. The resulting BL flow is therefore expected to sustain a spectrum of small-wavelength CFI modes while concentrating most of the spectral energy on the forced mode (Zoppini *et al.* 2022*a*). Subsequently, an SA with reference geometry and periodicity matching the wavelength of the forced mode is applied at

https://doi.org/10.1017/flo.2026.10048 Published online by Cambridge University Press

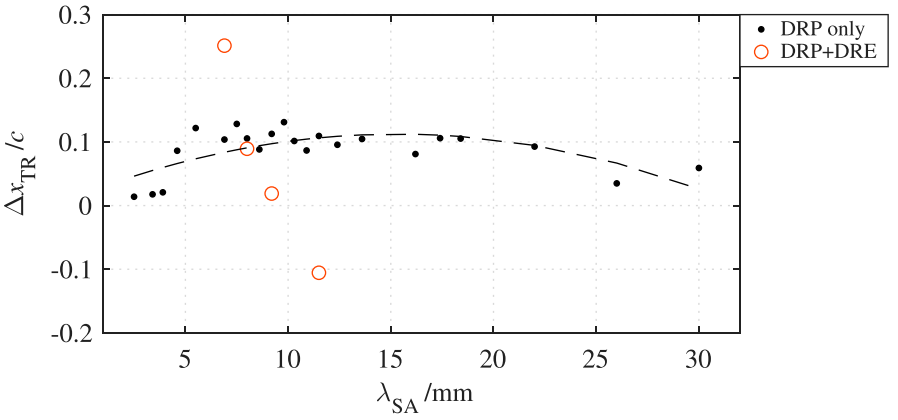

Figure 10. *$\Delta x_{\mathrm{TR}}/c$ extracted from IR images for DRP forcing only featuring SAs of various periodicities, λ_{SA}, and the corresponding second-order polynomial fit (- - -). For the DRP + DRE case, the SA wavelength corresponds to the wavelength of the DRE forced mode (A6, A7, A8 or A10).*

$x/c = 0.125$. It should be noted that the baseline BL for these cases corresponds to the flow forced solely by the DRP, whereas the control configurations consist of the combined action of the DRE (A6, A7, A8 or A10) and the SA tuned to the corresponding critical wavelength.

The resulting transition locations are displayed in Figure 10 as red circular markers. These results, once more, demonstrate that a sub-critical DRE, when combined with the corresponding SA wavelength, λ_{X}, extends the laminar portion of the flow up to $x/c \simeq 0.65$. This corresponds to $\Delta x_{\mathrm{TR}}/c \simeq 0.25$, a particularly noteworthy outcome given that it is achieved in a flow scenario representative of real flight conditions. Further studies are required to assess the robustness of this result with respect to SA geometry, DRP location and flow conditions; nevertheless, this estimate strongly suggests that the proposed technique holds significant potential for in-flight applications.

Substantial transition delay is also achieved under near-critical DRE forcing, whereas in the critical BL, the control effectiveness is reduced compared with the case of DRP alone. This is consistent with the fact that, when the DRP is active, the growth of the critical CFI mode is partially suppressed by the simultaneous amplification of small-wavelength modes. Conversely, with A8 applied near the leading edge, the growth of the λ_1 mode is promoted; in combination with the broader spectral content induced by the DRP, this leads to rapidly amplifying instabilities that break down earlier. A similar effect occurs with A10, where a super-critical CFI mode is excited and evolves alongside the most critical λ_1 mode. This configuration is the only one to produce transition advancement, i.e. a reduction of the laminar region relative to DRP forcing alone.

4.3. CFI amplitude as a function of SA periodicity

To validate the results provided by the IR investigation, for some of the considered roughness configurations, the local BL characteristics are estimated by analysing PIV measurements acquired at $x/c = 0.3$. Hereafter, the critical forcing case (A8) is considered in comparison to the flow field incurred by the application of the corresponding critical SA (A8, $N_{\mathrm{SA}} = 5$, $\lambda_{\mathrm{SA}} = 9.2\,\mathrm{mm}$). Figures 11a and 11c show the $\overline{w}_d$ velocity field for the baseline and controlled cases, respectively. Considered in combination with Figure 11e showing the relevant BL and disturbance velocity profiles, it appears that only a mild reduction of the BL disturbance is obtained in the controlled cases. Nonetheless, the disturbance profiles $\langle w \rangle_z$ show quantifiable CFI amplitude reduction, justifying the transition delay observed by IR imaging. In both the baseline and controlled cases, the $\langle w \rangle_z$ profile features a secondary peak indicative of the onset nonlinearities, which is reduced by applying the control SA.

https://doi.org/10.1017/flo.2026.10048 Published online by Cambridge University Press

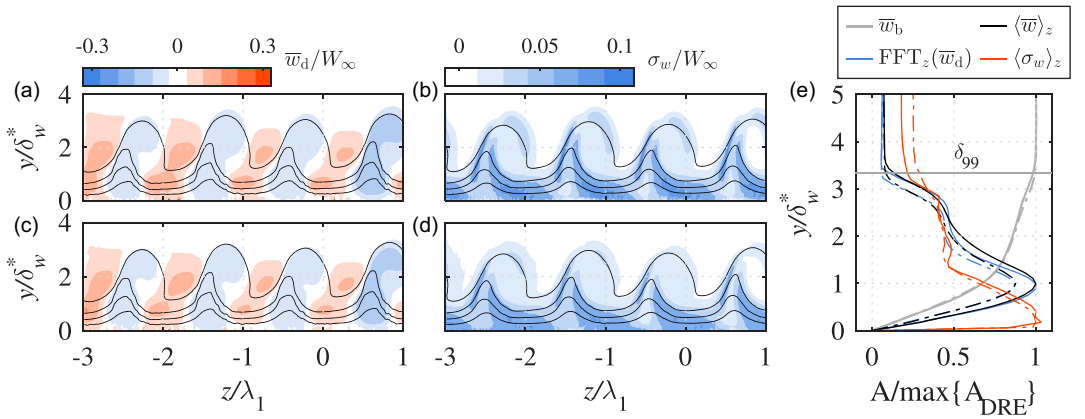

Figure 11. *(a) Mean velocity disturbance component, BL forced only critically (A8); (b) standard deviation, BL forced only critically (A8); (c) mean velocity disturbance component, BL forced critically (A8) and with an SA ($N_\mathrm{SA} = 5$, $\lambda_\mathrm{SA} = 9.2$ mm); (d) standard deviation, BL forced critically (A8) and with an SA ($N_\mathrm{SA} = 5$, $\lambda_\mathrm{SA} = 9.2$ mm); (e) mean BL profile, $\overline{w}_b$, standard deviations along the z directions of mean velocity, $\langle\overline{w}\rangle_z$, and of velocity standard deviation, $\langle\sigma_w\rangle_z$, as well as FFT amplitudes of the disturbance field. Solid lines correspond to forcing only with DRE A8, while dashed lines with DRE A8 and SA ($N_\mathrm{SA} = 5$, $\lambda_\mathrm{SA} = 9.2$ mm). Profiles are normalised with their maximum value.*

The presence of the SA also influences the unsteady component of the instabilities, here quantified by the standard deviation of the velocity field, σ_w, shown in Figures 11b and 11d. In the controlled BL, the overall standard deviation decreases, as evident from both the contours and the spanwise standard deviation profile, $\langle w' \rangle_z$, in Figure 11c. Nevertheless, in both cases, significant velocity fluctuations persist near the wall, spatially associated with type-III instabilities arising from interactions between primary stationary and primary travelling waves (Bonfigli & Kloker 2007; Malik *et al*. 1999; Serpieri & Kotsonis 2016; Wassermann & Kloker 2002). In contrast, the regions of elevated standard deviation observed in the outboard and inboard downwelling vortex regions coincide with high-shear layers where type-I and II secondary instabilities typically form (Malik *et al*. 1999; Wassermann & Kloker 2002). The application of the SA reduces σ_w in these regions, thereby delaying the onset and growth of secondary instabilities – an essential mechanism for achieving BL transition delay.

Spanwise FFT analysis of the $\overline{w}_d$ signal confirms that the dominant mode periodicity, along with its harmonics, is preserved in the presence of the SA (Figure 12a). This enables isolation and tracking of the dominant λ_1 mode, represented by its FFT shape function (blue line in Figure 11e). The shape function closely follows the disturbance profile, but with slightly reduced amplitude, as it reflects only the dominant CFI mode, whereas $\langle w \rangle_z$ includes contributions from all instabilities and disturbances in the BL. Furthermore, the zoomed-in subplot of the λ_1 spectral peak shows that all controlled cases decrease its amplitude, with the strongest reduction obtained for an SA wavelength of $\lambda_\mathrm{SA} = 9.2$ mm, i.e. corresponding to λ_X for A8.

By integrating the λ_1 mode shape function along y, the corresponding CFI amplitude (A_{λ_1}) is computed, providing a quantitative estimate of the damping and delaying effect of the SA. This value is shown in Figure 12b as A_diff, expressing the difference between the controlled and baseline reference amplitude as a percentage of the baseline case amplitude. In agreement with the previous discussions, the cases forced by λ_SA in the range of 8 mm to 11.5 mm lead to an amplitude reduction of the order of 10 %–15 % of the baseline case amplitude (which for the A8 forcing reaches values of 0.11 %W_∞). The amplitude reduction obtained for the other considered λ_SA is still significant, but reflects the lower transition delay observed for these cases (see Figure 9).

Comparable observations pertain to the sub-critical, near-critical and super-critical baseline and forced cases discussed in the previous section. For these cases, PIV acquisitions are only performed

https://doi.org/10.1017/flo.2026.10048 Published online by Cambridge University Press

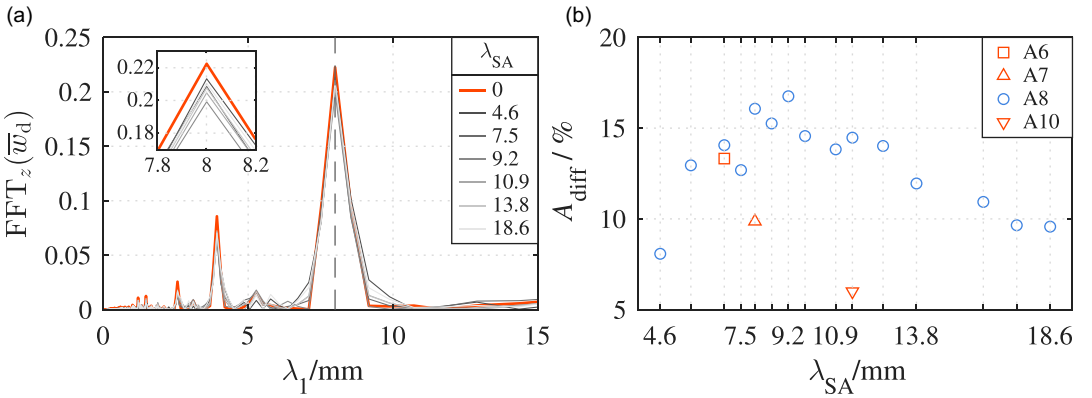

Figure 12. *(a) Spatial FFT spectra extracted at* $y/\overline{\delta_w^*} = 1$ *for the reference baseline case* ($\lambda_{SA} = 0$) *and selected controlled cases. (b) Amplitude reduction obtained in the controlled cases expressed as percentage difference with respect to the baseline case amplitude.*

for the flow field controlled by the corresponding critical SA. In all of the considered configurations, the presence of the SA has been found to preserve the dominant flow periodicity while damping the amplitude of the dominant mode. The resulting A_{diff} values are reported as coloured circles in Figure 12b, still providing significant reduction of the developing CFI amplitudes.

5. Concluding remarks

This study investigates the efficacy of spanwise-invariant roughness strip arrays (SAs) for laminar flow control application in cross-flow-dominated BL. The control configuration is composed of a repetition of two-dimensional roughness elements in the form of spanwise strips with various periodicity along the wing chord. The control capabilities of the considered geometries are estimated monitoring the BL transition location and its variations through IR thermography. In addition, local PIV provides information of the BL spectral content and on the CFI amplitude variation for the measured controlled BL cases.

SAs are applied in a DRE-forced BL, in which the forced CFI mode dominates the BL development. As a first step, the optimal geometry (i.e. amplitude, width and chord-wise location) of the SA for the current application is found. For this optimal geometry, the sensitivity to streamwise wavelength is investigated for a range of sub-critical, critical and super-critical BLs. In sub-critically forced BL, low sensitivity to the SA wavelength is observed, as all the considered configurations provide 8 %–10 % transition delay. Stronger sensitivity to SA periodicity is observed for critical and super-critical BLs, with stronger transition delay provided by those SA with λ_X comparable to the dominant CFI mode.

Such control capabilities are retained in the presence of enhanced distributed surface roughness, providing a scenario resembling the rough finishing of manufactured wing surfaces. Interestingly, in a DRP-forced BL, applying a control configuration that combines a DRE and an SA with corresponding critical streamwise wavelength provides transition delay when compared with the reference DRP-forced BL. This is particularly true for a sub-critically forced BL, where the combination with a corresponding critical λ_x SA provides up to 30 % transition delay. An analysis of the CFI amplitude as a function of SA periodicity corroborates these findings, showing the controlled BL scenarios retain the dominant CFI mode wavelength providing a reduction in its amplitude.

In summary, this study outlines the potential of suitably designed spanwise-uniform periodic roughness configurations for laminar flow control applications, with implications extending to real-flight scenarios. The performance metrics of the control system were demonstrated to be highly sensitive to the parametric variations of SA geometry. Nevertheless, the study acknowledges the limitations associated

https://doi.org/10.1017/flo.2026.10048 Published online by Cambridge University Press

with the available dataset, precluding a comprehensive understanding of the underlying flow mechanisms contributing to the observed transition delay. Consequently, future research endeavours will focus on conducting in-depth investigations to elucidate the governing flow mechanisms at play. In addition, the present configurations are idealised and do not represent a fully realistic operational environment. While real surfaces will inevitably contain localised defects (e.g. insect contamination or scratches), the present results suggest that the control mechanism itself is robust at the instability level, even if its practical realisation would require strategies to manage surface contamination.

Acknowledgements. We gratefully acknowledge Emiel Langedijk and Stefan Bernardy for their technical support.

Data availability statement. Raw data are available from the corresponding author.

Funding statement. The authors are grateful to the European Research Council for financially supporting this research through the GloWing Starting Grant (grant no. 803082). Open access funding provided by Delft University of Technology.

Declaration of interests. The authors declare no conflict of interest.

References

Barnes, C. J., Willey, C. L., Rosenberg, K., Medina, A., & Juhl, A. (2021). Initial computational investigation toward passive transition delay using a phononic subsurface. In *AIAA scitech 2021 forum* (p. 1454).

Baumann, M., Sturzebecher, D., & Nitsche, W. (2000). Active control of TS-instabilities on an unswept wing. In *Laminar-turbulent transition* (pp. 155–160). Springer.

Bippes, H. (1999). Basic experiments on transition in three-dimensional boundary layers dominated by crossflow instability. *Progress in Aerospace Sciences*, *35*(35), 363–412.

Boeing. (2013). Quarterly issue: Issue 49 quarter 01. Boeing Aero Magazine..

Bonfigli, G., & Kloker, M. (2007). Secondary instability of crossflow vortices: Validation of the stability theory by direct numerical simulation. *Journal of Fluid Mechanics*, *583*, 229–272.

Dagenhart, J. R., & Saric, W. S. (1999). *Crossflow stability and transition experiments in swept-wing flow*. NASA Center.

Deyhle, H., & Bippes, H. (1996). Disturbance growth in an unstable three-dimensional boundary layer and its dependence on environmental conditions. *Journal of Fluid Mechanics*, *316*, 73–113.

Dong, M., & Wu, X. (2016). A local scattering theory for the effects of isolated roughness on boundary-layer instability and transition: Transmission coefficient as an eigenvalue. *Journal of Fluid Mechnics*, *794*, 68–108.

Downs, R. S., & White, E. B. (2013). Free-stream turbulence and the development of cross-flow disturbances. *Journal of Fluid Mechanics*, *735*, 347–380.

Friederich, T. A., & Kloker, M. J. (2012). Control of the secondary cross-flow instability using localized suction. *Journal of Fluid Mechanics*, *706*, 470–495.

Gabor, D. (1946). Theory of communication. Part 1: The analysis of information. *Journal of the Institution of Electrical Engineers – Part III: Radio and Communication Engineering*, *93*(26), 429–441.

Hunt, L., & Saric, W. (2011). Boundary-layer receptivity of three-dimensional roughness arrays on a swept-wing. In: *41st AIAA fluid dynamics conference and exhibit*.

Hussein, M. I., Biringen, S., Bilal, O. R., & Kucala, A. (2015). Flow stabilization by subsurface phonons. *Proceedings of the Royal Society A: Mathematical, Physical and Engineering Sciences 471*, (*2177*), 20140928.

Ivanov, A. V., Mischenko, D. A., & Ustinov, M. V. (2018). Experimental investigation of laminar-turbulent transition control on swept-wing with help of oblique surface non-uniformities. *AIP Conference Proceedings*, *2027*(1), 030152.

Justiniano, E., Brown, L. M., White, E. B., Suryanarayanan, S., & Goldstein, D. B. (2024). Mitigation of roughness-induced boundary-layer transition on airfoils using shielding strips. *AIAA Journal*, *62*(7), 2476–2488.

Kendall, J. M. (1981). Laminar boundary layer velocity distortion by surface roughness: Effect upon stability. In *19th AIAA Aerospace Sciences Meeting* (AIAA Paper 81-0195), St. Louis.

Ladd, D. M. (1990). Control of natural laminar instability waves on an axisymmetric body. *AIAA Journal*, *28*(2), 367–369.

Lemarechal, J., Costantini, M., Klein, C., Kloker, M. J., Würz, W., Kurz, H. B. E., Streit, T., & Schaber, S. (2019). Investigation of stationary-crossflow-instability induced transition with the temperature-sensitive paint method. *Experimental Thermal and Fluid Science*, *109*, 109848.

Mack, L. M. (1984). Boundary-layer linear stability theory. Tech. Rep. 709., AGARD.

Malik, M. R., Li, F., Choudari, M. M., & Chang, C. L. (1999). Secondary instability of crossflow vortices and swept-wing boundary-layer transition. *Journal of Fluid Mechanics*, *399*, 85–115.

Messing, R., & Kloker, M. J. (2010). Investigation of suction for laminar flow control of three-dimensional boundary layers. *Journal of Fluid Mechanics*, *658*, 117–147.

https://doi.org/10.1017/flo.2026.10048 Published online by Cambridge University Press

Michelis, T., Head, A. J., & Colonna, P. (2024). Estimation of local Mach number in compressible flows of dense organic vapors using Gabor filters and Radon transforms for the post-processing of schlieren images. *Experiments in Fluids*, *65*, 185.
Michelis, T., de Koning, C., & Kotsonis, M. (2023a). On the interaction of Tollmien–Schlichting waves with a wall-embedded Helmholtz resonator. *Physics of Fluids*, *35*(3), 034104.
Michelis, T., Putranto, A. B., & Kotsonis, M. (2023b). Attenuation of Tollmien–Schlichting waves using resonating surface-embedded phononic crystals. *Physics of Fluids*, *35*(4), 044101.
Milling, R. W. (1981). Tollmien–Schlichting wave cancellation. *Physics of Fluids*, *24*(5), 979.
Müeller, B., & Bippes, H. (1989). Experimental study of instability modes in a three-dimensional boundary layer. Tech. Rep. AGARD CP, NATO AGARD.
Park, S., Hristov, G., Balasubramanian, S., Goza, A., Ansell, P. J., & Matlack, K. (2022). Design and analysis of phononic material for passive flow control, forum. In *AIAA AVIATION 2022 forum*. American Institute of Aeronautics and Astronautics.
Radeztsky, R. H., Reibert, M. S., & Saric, W. S. (1999). Effect of isolated micron-sized roughness on transition in swept-wing flows. *AIAA Journal*, *37*(11), 1370–1377.
Reibert, M., Saric, W. S., Carrillo, Jr. R., & Chapman, K. (1996). Experiments in nonlinear saturation of stationary crossflow vortices in a swept-wing boundary layer. In: *34th Aerospace Sciences Meeting and Exhibit*. American Institute of Aeronautics and Astronautics.
Reynolds, O. (1883). Xxix. An experimental investigation of the circumstances which determine whether the motion of water shall be direct or sinuous, and of the law of resistance in parallel channels. *Philosophical Transactions of the Royal Society of London*, *174*, 935–982.
Saric, W. S., Carpenter, A. L., & Reed, H. L. (2011). Passive control of transition in three-dimensional boundary layers, with emphasis on discrete roughness elements. *Philosophical Transactions of the Royal Society A: Mathematical, Physical and Engineering Sciences*, *369*(1940), 1352–1364.
Saric, W. S., Carrillo, Jr., & Reibert, M. S. (1998). Leading-edge roughness as a transition control mechanism. In: *36th AIAA aerospace sciences meeting and exhibit*.
Saric, W. S., Reed, H. L., & White, E. B. (2003). Stability and transition of three dimensional boundary layers. *Annual Review of Fluid Mechanics*, *35*(1), 413–440.
Schlichting, H., & Gersten, K. (2017). *Boundary-layer theory*. Springer.
Schubauer, G. B., & Skramstad, H. K. (1947). Laminar boundary-layer oscillations and transition on a flat plate. *Journal of Research of the National Bureau of Standards*, *38*, 251.
Serpieri, J. (2018). Cross-flow instability (PhD thesis, Technische Universiteit Delft).
Serpieri, J., & Kotsonis, M. (2015). Design of a swept wing wind tunnel model for study of cross-flow instability. In *33rd AIAA applied aerodynamics conference*. American Institute of Aeronautics and Astronautics.
Serpieri, J., & Kotsonis, M. (2016). Three-dimensional organisation of primary and secondary crossflow instability. *Journal of Fluid Mechanics*, *799*, 200–245.
Sturzebecher, D., & Nitsche, W. (2003). Active cancellation of Tollmien–Schlichting instabilities on a wing using multi-channel sensor actuator systems. *International Journal of Heat and Fluid Flow*, *24*(4), 572–583.
Suryanarayanan, S., Goldstein, D. B., Berger, A. R., White, E. B., & Brown, G. L. (2020). Mechanisms of roughness-induced boundary-layer transition control by shielding. *AIAA Journal*, *58*(7), 2951–2963.
Tempelmann, D., Schrader, L. U., Hanifi, A., Brandt, L., & Henningson, D. S. (2012). Swept wing boundary-layer receptivity to localized surface roughness. *Journal of Fluid Mechanics*, *711*, 516–544.
Tol, H. J., Kotsonis, M., & Visser, C. C. De (2019a). Pressure output Feedback control of tollmien-schlichting waves in Falkner-skan boundary layers. *AIAA Journal*, *57*(4), 1538–1551.
Tol, H. J., de Visser, C. C., & Kotsonis, M. (2019b). Experimental model-based estimation and control of natural tollmien-schlichting waves. *AIAA Journal*, *57*(6), 2344–2355.
Wassermann, P., & Kloker, M. (2000). DNS-investigations of the development and control of crossflow vortices in a 3-D boundary-layer flow. In *Laminar-turbulent transition* (pp. 565–570). Springer.
Wassermann, P., & Kloker, M. (2002). Mechanisms and passive control of crossflow-vortex-induced transition in a three-dimensional boundary layer. *Journal of Fluid Mechanics*, *456*, 49–84.
H., Xu, Sherwin, S. J., Hall, P., & Wu, X. (2016). The behaviour of Tollmien–Schlichting waves undergoing small-scale localised distortions. *Journal of Fluid Mechanics*, *792*, 499–525.
Zoppini, G. (2023). Receptivity of swept wing boundary layers to surface roughness (PhD thesis, Delft University of Technology).
Zoppini, G., Michelis, T., Ragni, D., & Kotsonis, M. (2022a). Cancellation of crossflow instabilities through multiple discrete roughness elements forcing. *Physical Review Fluids*, *7*(12), 123902.
Zoppini, G., Westerbeek, S., Ragni, D., & Kotsonis, M. (2022b). Receptivity of crossflow instability to discrete roughness amplitude and location. *Journal of Fluid Mechanics*, *939*, A33.

Cite this article: Zoppini G., Kotsonis M. and Michelis T. (2026). Control of stationary cross-flow instabilities using periodic arrays of spanwise-invariant roughness strips. *Flow*, *6*, E11. https://doi.org/10.1017/flo.2026.10048